Localized Compaction in Tuffeau de Maastricht: Experiments and Modeling

Athanasios Papazoglou, Ghassan Shahin, Ferdinando Marinelli, Christophe Dano, Giuseppe Buscarnera, Gioacchino Viggiani

Localized compaction in Tuffeau de Maastricht: experiments and modeling

A. Papazoglou, G. Shahin, F. Marinelli, C. Dano, G. Buscarnera and G. Viggiani

Abstract This paper presents an experimental and constitutive study of compaction banding in Tuffeau de Maastricht, a bioclastic sedimentary limestone exhibiting up to 52% of porosity. An elasto-plastic constitutive model is used to simulate the mechanical behavior of the limestone within the compaction localization regime. It is shown that the simulated macroscopic behavior is in good agreement with the experimental data. In addition, image processing tools have been used to perform full-field measurements elucidating the mechanics of initiation and propagation of localized compaction zones. These findings emphasize the complex nature of localized compaction in porous rocks and represent a preliminary step towards the integrated use of multi-scale testing and mechanical modeling for their characterization across scales.

1 Introduction

Compaction bands have been observed in different kinds of materials (*e.g.,* rocks, soils, metallic foams, cellular materials). They are usually promoted by a relatively high porosity, as well as by high mean stress levels. However, the inelastic mechanisms controlling localized compaction at the micro-scale can differ from one material to another. For instance, buckling of thin walls has been observed in metallic foams or honeycomb structures. In the case of geomaterials, due to their natural variability, the microstructural origin of compaction localization is still an open question, often complicated by the coexistence of multiple inelastic processes (*e.g.,* pore

A. Papazoglou, C. Dano and G. Viggiani
Laboratoire 3SR, Université Grenoble Alpes, Grenoble, e-mail: athanasios.papazoglou@3sr-grenoble.fr

G. Shahin, F. Marinelli and G. Buscarnera
Department of Civil and Environmental Engineering, Northwestern University, Evanston, e-mail: ghassanshahin@u.northwestern.edu

collapse, grain crushing, degradation of cementation bonds). Full-field non destructive measurements have thus the potential to identify these micro-mechanisms and assess their relative role.

2 Material tested and experimental set-up

The material studied in this work is Tuffeau de Maastricht, a limestone that was formed by sediments transported and deposited in a marine environment during the Late Cretaceous [2, 3]. The material microstructure consists of carbonate bioclasts and shell fragments. Although the average grain size is about 100-200 μm, bigger fossils and inclusions can also be observed. Such constituents are bonded together by a weak cementation, which mainly occurs at contact points around echinoderm bioclasts. The pore structure of Tuffeau de Maastricht is characterized by high porosity (up to 52%), which is mainly due to the intragranular porosity within the shell fragments (see Fig. 1) [5, 6]. The weak cementation, combined with the high porosity, results in a soft rock with low stiffness and strength (unconfined compressive strength is less than 5 MPa) [11]. Figure 1 illustrates the complex structure of the selected rock at the micro scale, where both intergranular voids and bioclasts can be recognized (black color corresponds to pores).

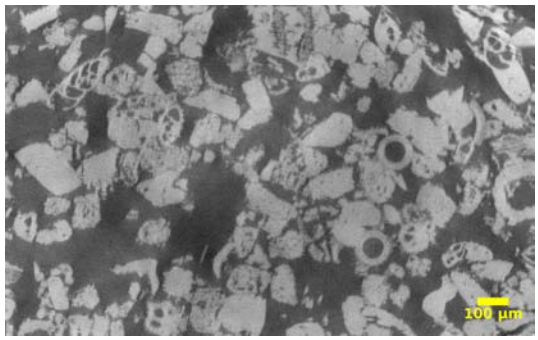

Fig. 1 CT scan of Tuffeau de Maastricht at 1μm resolution, revealing intragranular porosity and bioclasts variability.

The testing campaign consisted of an isotropic compression test and a number of triaxial compression tests on dry specimens. For this purpose, cylindrical specimens of 2:1 height-diameter ratio and 10mm diameter were prepared and tested in a miniaturized triaxial compression apparatus allowing for in situ x-ray scans with a voxel size of 13 microns. Note that since the specimens were tested dry, the volumetric strain was directly measured from the 3D images obtained throughout the tests. The isotropic compression test was conducted by increasing step-by-step the confining pressure. The response obtained in the plane mean stress (p) - volumetric strain (ε_v) can be divided in two segments. The first segment is quasi-linear until a limit stress, at which a sudden reduction in volume is observed (see Fig. 3(a)).

The triaxial tests were performed at different confining pressures ranging from 0 (no confinement) to 4.0 MPa (see Fig. 2). Loading was interrupted at various points and x-ray scans were performed. The radiographs obtained were then used to reconstruct 3D tomographic volumes. In addition to the compression tests reported in Figure 2, a further experiment at 4.0 MPa confinement was conducted, to a much higher axial strain (almost 50%). Figure 5(a) shows the deviator stress versus axial strain, as well as the volumetric response of the material. The material exhibits an initial linear phase portion and then a plateau of deviator stress. After 14% axial strain, the deviator stress starts to increase again.

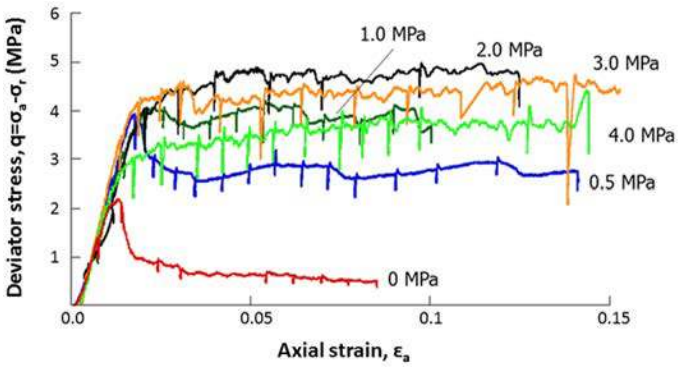

Fig. 2 Curves of deviator stress ($q = \sigma_a - \sigma_r$) vs. axial strain obtained from triaxial compression experiments at different confining pressures.

3 Constitutive modeling

A constitutive model based on earlier contributions by Nova and co-workers [7, 9, 12] is here selected to reproduce the plastic collapse occurring in high-porosity rocks under isotropic and/or shear loading. Yield surface f and plastic potential g are expressed as follows [9]:

$$\left.\begin{matrix} f \\ g \end{matrix}\right\} = \frac{p}{p_c^\star} - \frac{\left(1+\frac{\eta^\star}{M_h K_2}\right)^{\frac{K_2}{(1-\mu_h)(K_1-K_2)}}}{\left(1+\frac{\eta^\star}{M_h K_1}\right)^{\frac{K_1}{(1-\mu_h)(K_1-K_2)}}} \qquad \eta^\star = \frac{q}{p+p_t} \tag{1}$$

$$K_{1/2} = \frac{\mu_h(1-\alpha_h)}{2(1-\mu_h)}\left(1 \pm \sqrt{1-\frac{4\alpha_h(1-\mu_h)}{\mu_h(1-\alpha_h)^2}}\right), \tag{2}$$

These functions are characterized by distinct sets of shape parameters M_h, μ_h, and α_h (with the subscript h referring to either f or g). The size of the yield surface is governed by the parameter $p_c^\star = p_s + p_m + p_t$, where p_s reflects the state of material compaction, while p_m simulates the effect of inter-particle bonding. Finally, p_t, which defines the tensile strength of the material, is assumed to be proportional to p_m (*i.e.,* $p_t = \kappa\, p_m$). The mechanical response within the yield surface has been simulated with isotropic linear elasticity, while the hardening/softening characteristics are governed by the following equations:

$$\dot{p}_s = \frac{p_s}{B_p}\dot{\varepsilon}_v^p \qquad \dot{p}_m = -\rho_m p_m(|\dot{\varepsilon}_v^p| + \xi_m \dot{\varepsilon}_q^p) \tag{3}$$

where B_p, ρ_m and ξ_m are constitutive parameters. From Equations 3 it can be readily noted that the interplay between the hardening of p_s in the compaction regime and the reduction of p_m may result in either contraction or expansion of the yield surface.

An isotropic compression test has been used to calibrate B_p and ρ_m (Fig. 3(a)). Given the lack of data about the isotropic hardening of the Tuffeau de Maastricht at high pressures, the value of B_p has been defined on the basis of evidences available for a calcareous rock of similar porosity (*i.e.,* the Gravina calcarenite tested by [8]). This choice has allowed us constraining the plastic compressibility of the fully destructured material, as well as the magnitude of ρ_m and the initial values of p_m and p_s. The shape parameters of the yield function (*i.e.,* α_f, μ_f, M_f and κ in

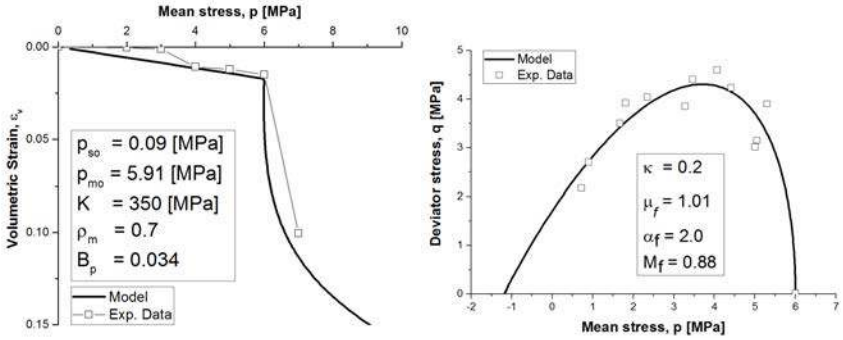

(a) (b)

Fig. 3 Calibration of (a) the hardening parameters, and (b) initial yield surface. The values of the calibrated parameters are given in the relevant plot.

Fig. 3(a)) have been calibrated by fitting the yielding points extracted from Fig. 2), and the resulting function is depicted in Fig 3(b). Finally, the shape parameters of the plastic potential (μ_g, α_g, and M_g) have been defined by means of the dilatancy function $d = d(\eta^\star)$, *i.e.* the ratio between the increments of volumetric and deviatoric plastic strains. Data used for this purpose is extracted from the triaxial test in Fig. 5(a). The results are illustrated in Fig. 4 where, for comparison purposes, the

$d(\eta^\star)$ relationship which would result from the use of an associated plastic flow rule is also reported. This comparison emphasizes the pronounced non-associativity of the Tuffeau de Maastricht, which usually underscores a non-negligible potential to develop strain inhomogeneity.

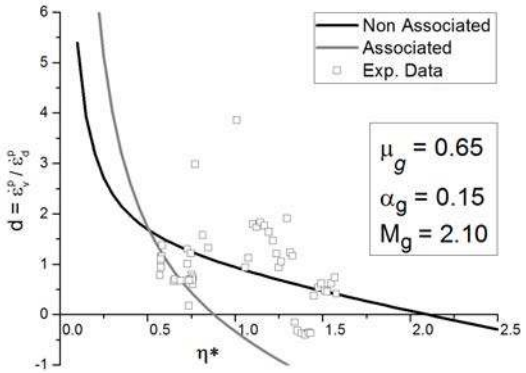

Fig. 4 Calibration of the dilatancy function $d(\eta^\star)$ by using the experimental data plotted in Fig. 5(a) (the dilatancy function corresponding to associative plasticity is also plotted for comparison purpose).

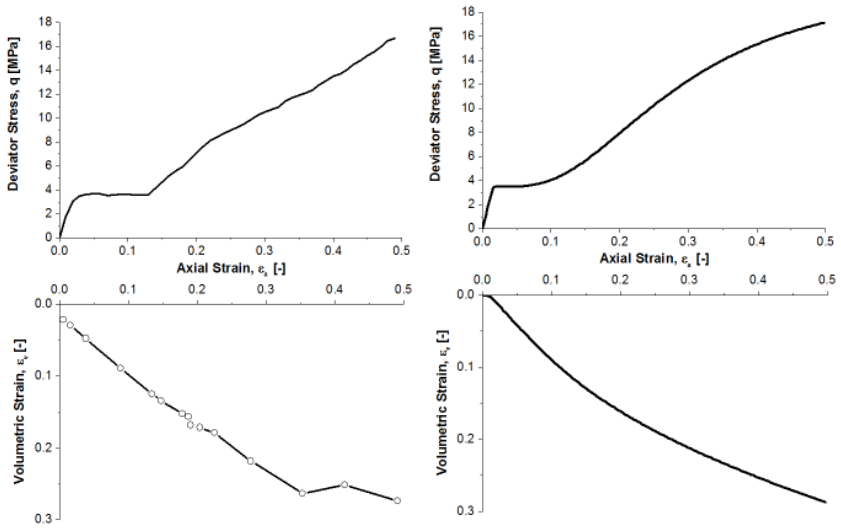

(a) (b)

Fig. 5 Comparison between experimental data (a) and numerical results (b) for a triaxial test performed at 4.0 MPa of confinement pressure; simulation performed with G=80 MPa and ξ_m=0.0.

The performance of the calibrated model has been tested by simulating a triaxial test at 4.0 MPa confining pressure. The computed material point response in Fig. 5(b)

can be compared to the corresponding experimental result in Fig. 5(a). It can be readily noted that by adequately constraining the proportion between hardening and softening terms it is possible to simulate realistically the transition from a perfectly plastic flow in the vicinity of the yielding point to a considerable re-hardening at larger strains. Despite such satisfactory agreement between data and computations, it is worth remarking that this comparison is based on a material-point assessment of the rock response. As a result, it should be regarded as a first-order approximation of the constitutive properties susceptible to further refinements based on the detailed full-field observations discussed in the next section.

4 Measured fields of porosity and incremental strain

Although the numerical model captures the global mechanical response of the material, the characterization of local inelastic processes requires a more detailed inspection. For this purpose, image analysis was performed on the triaxial test at a 4.0 MPa confining stress, to track the initiation and evolution of localized compaction during the above mentioned compression experiments.

In this work, the porosity was measured locally by working on image gray-scale level through sub-volumes defined within the reconstructed images. These measurements, obtained using a code developed by [1], represent the volume of the voids within the sub-volume. The appropriate (representative) sub-volume size has been decided by analyzing the measurements of porosity and its fluctuations as a function of the sub-volume size. Since the measurements become less sensitive to the cube size and converge to the global porosity of the specimen as the size of the sub-volume increases, a fixed value of 55 voxels has been chosen as representative elementary volume (REV).

3D Digital Image Correlation (DIC) was also performed to measure the evolution of strain field in the specimen while it deforms under loading, using the code "TomoWarp2" (see [13] for details).

Figure 6 shows vertical slices of the 3D strain maps obtained with DIC. The scalar quantity mapped in the figure is the maximum shear strain. Note that this is incremental. The localization appears at the bottom and top of the specimen before the peak at 2-3% of axial strain and extends towards the middle. The porosity map (Fig. 7) indicates the initial high porosity of the material and its evolution during the loading. This densified zone starts from the bottom and top and increases in thickness until it covers the whole specimen. At the end of the deviator stress plateau at 14% axial strain, the entire specimen has a porosity of 38%. It should be noticed that the strain maps clearly point out that the propagation of localized compaction zones coincides with the initial plateau of deviator stress, while the achievement of a homogeneously compacted state marks the onset of re-hardening.

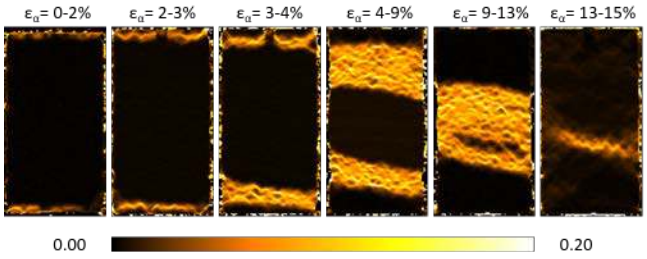

Fig. 6 Vertical slices in different increments of stain, results of the 3D-DIC in terms of maximum shear strain.

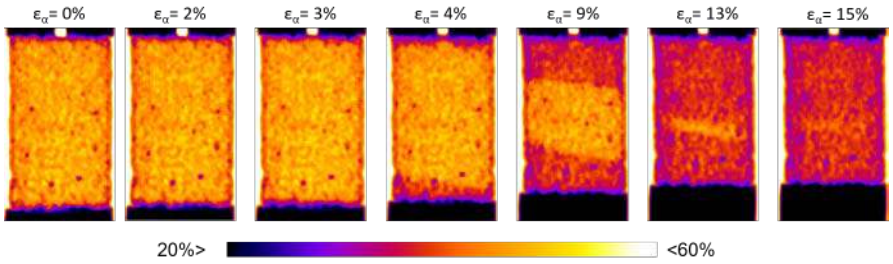

Fig. 7 Vertical slices through the measured 3D field of porosity in different configuration of the triaxial compression test at 4.0 MPa confining pressure. Note that the porosity decreases up to 26% from the initial value (52% - 38%).

5 Discussion and conclusions

Localized compaction in Tuffeau de Maastricht has been studied through experiments and constitutive analyses. Triaxial compression tests conducted at different confining pressures have generated a post-yielding response characterized by nearly constant deviator stress and considerable compaction. It has been shown that the continuation of the compression test beyond the post-yielding plateau causes a transition from a perfectly plastic stage to a noticeable re-hardening. These evidences have been interpreted through an elasto-plastic model relying on feedbacks between plastic compaction (hardening terms) and loss of structure (softening terms). The proportion between such feedbacks has been constrained through evidences of plastic collapse under isotropic conditions, thus generating a set of parameters reproducing successfully the transition from perfectly plastic flow to compaction-driven re-hardening. Such satisfactory agreement between data and computations has been achieved by enforcing plastic non-normality in the cap region, *i.e.,* a feature which usually underpins a non-negligible potential for strain inhomogeneity. The latter possibility has been assessed by full-field measurements collected by x-ray imaging and 3D-DIC, which identified successive formations of compaction bands moving from the boundaries towards the center of the sample until achieving a uniformly

compacted state which precedes the onset of re-hardening. Such findings illustrate the complex nature of the processes that characterize the response of porous rocks such as the Tuffeau de Maastricht, thus warranting further analyses elucidating the microscopic origin of localized compaction in this material, as well as the enhancement of their constitutive description through microstructural attributes reflecting the alteration of their pore networks.

References

1. E. Andò. *Experimental investigation of microstructural changes in deforming granular media using x-ray tomography*. PhD thesis, Université de Grenoble, 2013.
2. T. Baxevanis, E. Papamichos, O. Flornes, and I. Larsen. Compaction bands and induced permeability reduction in tuffeau de maastricht calcarenite. *Acta Geotechnica*, 1(2):123–135, 2006.
3. R. F. Bekendam. *Pillar stability and large-sacle collapse of abandoned room and pillar limestone mines in South-Limburg, the Netherlands*. TU Delft, Delft University of Technology, 1998.
4. A. Das and G. Buscarnera. Simulation of localized compaction in high-porosity calcarenite subjected to boundary constraints. *International Journal of Rock Mechanics and Mining Sciences*, 71:91–104, 2014.
5. R. Dreesen and M. Dusar. Historical building stones in the province of limburg (ne belgium): role of petrography in provenance and durability assessment. *Materials Characterization*, 53(2):273–287, 2004.
6. C. Dubelaar, M. Dusar, R. Dreesen, W. Felder, and T. Nijland. Maastricht limestone: a regionally significant building stone in belgium and the Netherlands. extremely weak yet time-resistant. In *Proceedings of the international heritage weathering and conservation conference. Taylor & Francis Group, London*, pages 9–14, 2006.
7. A. Gens and R. Nova. Conceptual bases for a constitutive model for bonded soils and weak rocks. *Geotechnical engineering of hard soils-soft rocks*, 1(1):485–494, 1993.
8. R. Lagioia and R. Nova. An experimental and theoretical study of the behaviour of a calcarenite in triaxial compression. *Géotechnique*, 45(4):633–648, 1995.
9. R. Lagioia, A. Puzrin, and D. Potts. A new versatile expression for yield and plastic potential surfaces. *Computers and Geotechnics*, 19(3):171–191, 1996.
10. F. Marinelli and G. Buscarnera. Parameter calibration for high-porosity sandstones deformed in the compaction banding regime. *International Journal of Rock Mechanics and Mining Sciences*, 78:240–252, 2015.
11. D. Ngan-Tillard, W. Verwaal, A. Mulder, H. Engin, and R. Ulusay. Application of the needle penetration test to a calcarenite, Maastricht, the Netherlands. *Engineering Geology*, 123(3):214–224, 2011.
12. R. Nova, R. Castellanza, and C. Tamagnini. A constitutive model for bonded geomaterials subject to mechanical and/or chemical degradation. *International Journal for Numerical and Analytical Methods in Geomechanics*, 27(9):705–732, 2003.
13. E. Tudisco, S. Hall, E. M. Charalampidou, N. Kardjilov, A. Hilger, and H. Sone. Full-field measurements of strain localisation in sandstone by neutron tomography and 3d-volumetric digital image correlation. *Physics Procedia*, 69:509–515, 2015.